Journal of Visualization, Vol. 7, No. 3 (2004) 179-186

POD Analysis of Near-wake Structures of an Elliptic Cylinder Adjacent to a Free Surface

Daichin* and Lee, Sang Joon *

* Dept. of Mechanical Engineering, Pohang University of Science and Technology, Pohang, 790-784, Korea.
E-mail: sjlee@postech.ac.kr

Received 3 November 2003
Revised 1 March 2004

Abstract : The POD (Proper Orthogonal Decomposition) method was used to investigate the near-wake behind an elliptic cylinder located under a free surface. For two different depths of cylinder submergence, the first four eigenmodes of the flow field were calculated and their structures were analyzed. The first four eigenmodes reveal the details about the global mean flow structure, with the large-scale structure being mainly related to the most energetic flow motion. The convergence of accumulated eigenvalues shows a slight dependence on the number of instantaneous velocity fields used in POD analysis.

Keywords : POD, Elliptic cylinder, Near-wake, Free surface.

1. Introduction

Among various types of bluff body, the elliptic cylinder can be considered as a general configuration representing a wide range of geometrical shapes; by varying the cross-sectional axis ratio (**AR**) of an elliptic cylinder, a body can be transformed from a circular cylinder (**AR**=1) to a flat plate (**AR**=∞). Therefore, the flow around an elliptic cylinder might be expected to exhibit flow characteristics between those of a circular cylinder and a flat plate. Previous studies revealed that the flow structure around elliptic cylinders changes considerably with AR and angle of attack. Here, the AR of an elliptic cylinder is defined as the ratio of the major axis (**A**) to the minor axis (**B**). Modi and Wiland (1970) carried out an experimental study of the organized wake structure behind elliptic cylinders with axis ratios of **AR**=1.25 and 1.67 with varying the angle of attack. They found that, as the angle of attack was increased, the ratio of the lateral to the longitudinal spacing of the wake gradually decreased. Choi and Lee (2000) investigated the flow around an elliptic cylinder (**AR**=2) embedded in a turbulent boundary layer with varying the gap ratio (**h*=H/B**), defined as the ratio of the submergence depth (**H**) to the minor axis (**B**) of the elliptic cylinder. As the gap ratio was increased, the drag coefficient increased but the lift coefficient decreased. The drag coefficient was found to be about half of that of the circular cylinder having the same cross-sectional area.

In contrast to the considerable attention that has been devoted to the flow around elliptic cylinders near a solid boundary, the flow interaction between a free surface and the wake behind a nearby elliptic cylinder has received relatively little attention. When a cylinder is located near a free surface, the flow structure is completely different from that of the same cylinder in a uniform flow. One effective method for investigating complex flows containing large-scale organized structure and turbulent structure, such as the flow around a cylinder near a free surface, is POD (Proper

Orthogonal Decomposition) analysis (Lumley et al., 1993). The POD analysis can extract flow pattern based on the consideration of kinetic energy. It can be used to investigate the dominant coherent structure from instantaneous turbulent flow fields. In this study, we use the POD method to elucidate the dominant flow structure of the near wake behind an elliptic cylinder placed under a free surface. The POD analysis was performed for a time series of instantaneous velocity fields obtained by PIV technique.

2. The experimental set-up

Experiments were carried out in a circulating water channel (CWC) with a test-section size of 300 mm^W×250 mm^H ×1500 mm^L. Figure 1 shows a schematic diagram of the experimental set-up and coordinate system used in this study. The elliptic cylinder was mounted horizontally beneath the free surface, 800 mm downstream of the entrance of the CWC test section. An elliptic cylinder with an axis ratio of **AR**=2 was used in all experiments. The submergence depth (**H**) is defined as the gap between the cylinder upper surface and the free surface. The gap ratio (**h*=H/B**) is defined as the ratio of the submergence depth (**H**) to the minor axis (**B**) of the elliptic cylinder. The major and minor axes of the elliptic cylinder are 28.2mm and 14.1mm, respectively. The span (**W**) of the test cylinder is 300 mm, and the shape factor (**W/B**) is greater than 25. Since the shape factor of the experimental model is larger than the nominal value showing 2-D flow structure, the three-dimensional flow effect is nearly negligible in the central plane of the near wake. Flow patterns for two gap ratios, **h*** =0.3 and 0.6, are discussed in this paper. The coordinates **X** and **Y** denote the streamwise and vertical distances from the center of the elliptic cylinder, respectively. The free-stream flow velocity was fixed at $\mathbf{U}_0$= 0.20 m/s during the experiments. The Reynolds number based on the minor axis of the cylinder is Re=2800.

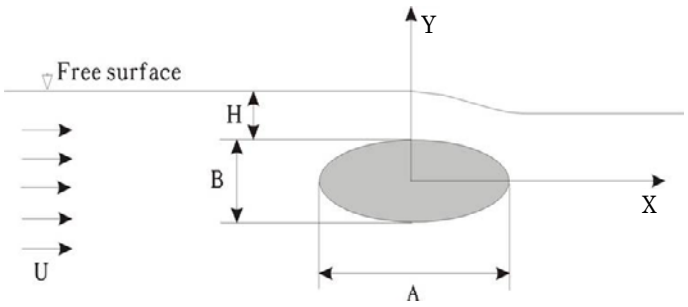

Fig. 1. Schematic diagram of the experimental set-up and coordinate system.

Instantaneous velocity fields were measured using a single-frame double-exposure PIV system. This system consisted of a high-resolution CCD camera of 2k×2k pixels resolution, a dual-head Nd:YAG laser, a synchronizer, and optics. The Nd:YAG laser provided a maximum energy of 25 mJ per pulse. The CCD camera has a single-frame double-exposure mode with an internal frame transfer feature. The laser and camera were synchronized using a delay generator (BNC 555-2). The details of the single-frame PIV system and its measurement uncertainty are described in Shin et al. (2000).

Vestosint®1118 particles with a mean diameter of 37 μm were seeded into the working fluid as tracer particles. The central cross-section of the flow around the elliptic cylinder was illuminated from the bottom of the cylinder at a slanted angle. As a result of this configuration, clear particle images could not be obtained in the region above the cylinder because the cylinder blocked the laser light sheet. For each experimental condition, 400 instantaneous velocity fields were obtained at a sampling rate of 4 fps (frames per second). The interrogation window size was 64 × 64 $pixels^2$ with 50% overlapping. Therefore, velocity vectors were calculated for every 32 pixels and the corresponding spatial resolution was 1.09×1.09 mm^2. Since the accuracy of POD data strongly depends on the quality of the original PIV data, the instantaneous velocity field data were carefully post-processed to get reliable POD results. The error vectors in PIV velocity maps were removed using the error vector detecting routine. The removed error vectors were replaced with the help of interpolation of nearby correct vectors, and then the smoothing process was employed to remove

noisy data. The interpolated and replaced vectors were checked using the continuity equation. After these post-processing routines, all instantaneous velocity fields were ensemble averaged to obtain spatial distributions of turbulent statistics such as mean velocity and turbulent kinetic energy.

3. POD

The basic principle of POD is straightforward. Let us consider an ensemble of scalar fields, $\{u^k\}$, where each field is a function $u=u(x)$ defined on the domain $0 \leq x \leq 1$. To obtain good representations of the members of $\{u^k\}$, each u need to be projected onto candidate basis functions. Therefore, we have to find a basis $\{\phi_j\}_{j=1\sim\infty}$ that is optimal for the data set $\{u^k\}$. Members of the data set can be represented as follows:

$$u_N(x) = \sum_{j=1}^{N} a_j \phi_j(x) \tag{1}$$

where a_j is the coefficient of projection. That is, we should choose ϕ to maximize the averaged projection of u onto ϕ, suitably normalized as follows:

$$\max_{\phi} \frac{\left\langle \left|(u,\phi)\right|^2 \right\rangle}{\left\|\phi\right\|^2} \tag{2}$$

where $\left|(u,\phi)\right|$ denotes the modulus and $\left\|\phi\right\|$ is the norm: $\left\|f\right\| = (f,f)^{1/2}$.

Maximizing this inner product leads to the solution of the following eigenvalue problem:

$$\iint_D R(x,x') \cdot \phi(x') dx' = \lambda \phi \tag{3}$$

where D represents the 2-dimensional domain of the velocity fields, and the function R is the averaged two-point correlation tensor, defined as $R_{i,j}(x,x') = \left\langle u^i(x) \cdot u^j(x') \right\rangle$. However, R is an $N \times N$ matrix, where $N=2 \times n$ (for a velocity field containing n vectors), and hence the dimension of R rapidly increases with increasing vector number such that, for flow fields with more than 1000 vectors, Equation (3) is difficult to solve with current computers. Sirovich (1987) proposed an equivalent approach, known as the *method of snapshots*, which utilizes the fact that the matrix $R(x, x')$ represents a degenerate kernel, and that the eigenfunctions can be expressed as admixtures of the instantaneous velocity fields:

$$R_{i,j}(x,x') = \frac{1}{M} \sum_{j=1}^{M} u^i(x) \cdot u^j(x) \tag{4}$$

where M is the number of ensembles, $\{u^k\}$, of instantaneous velocity fields. Therefore, the eigenfunctions ϕ can be expressed in the following form:

$$\phi = \sum_{k=1}^{M} A_k u^k \tag{5}$$

Combining Equations (3), (4), and (5) transforms the problem to the eigenvalue problem having the form $C \cdot A = \lambda \cdot A$; here C is an $M \times M$ matrix defined as $C_{i,j} = \sum_{m=1}^{n} u^i(x_m) \cdot u^j(x_m)$, where n is the total number of vectors in the velocity field. The ith eigenvalue of this system represents the coefficient used in Equation (5) to build the ith model function of the flow. Using this scheme, we can reduce the number of computations required to reach the solution.

After calculating all the eigenmodes $\{\phi_j\}$, each instantaneous velocity field can be reconstructed as a linear combination of modes:

$$u^i = \sum_{j}^{M} a_{i,j} \phi_j \tag{6}$$

Where the reconstruction coefficient $a_{i,j}$ has the dimension of velocity, because $\{\phi_j\}$ is an orthogonal

base. It can be obtained by projecting the raw velocity fields onto the POD basis:

$$a_{i,j} = (u^i, \phi_j) \tag{7}$$

The order of the eigenvalues is such that $\lambda_i > \lambda_{i+1}$. Since $R(x, x')$ is non-negative, the eigenvalues are positive ($\lambda_i > 0$). The eigenvalue λ_i represents twice the kinetic energy at each mode ϕ_j. It provides the energy rate of the flow structure, projected onto the mathematical basis represented by the associated eigenfunction. The contribution of each eigenmode depends on the magnitude of corresponding eigenvalue, i.e. the quantitative information of eigenvalues estimates the percentage contribution of kinetic energy contained in the flow field. The turbulence energy production containing large kinetic energy can be evaluated from the eigenvalues at a few initial eigenmodes. However, it is not easy to evaluate the dissipation process, because it has very small kinetic energy. The global flow structure can be reconstructed by linear combination of the most energetic eigenmodes. The POD analysis is a useful tool for extracting dominant coherent structures embedded in complicated flow fields.

4. Results and discussion

Figure 2 shows the mean velocity fields obtained by ensemble averaging 400 instantaneous velocity fields and the contour plots of the turbulent kinetic energy for gap ratios of **h***=0.3 and 0.6. For the smaller gap ratio of **h***=0.3, a jet-like flow is formed in the gap region between the cylinder and the free surface. The jet-like flow declines downward and merges with the mixing layer developed from the bottom surface of the cylinder, forming counter-rotating vortices at both sides of the jet. Due to active mixing with the jet flow, the ambient fluid is entrained into the wake to a greater extent. This causes a reverse flow in the region near the free surface. When the gap ratio is increased to h*=0.6, the gap blocks the flow to a lesser extent, and the jet flow attaches onto the free surface. The general flow pattern is similar to that of the wake behind a cylinder in an unbounded medium. Vortices are shed alternately from the upper and lower sides of the cylinder, although the flow speeds at both sides of the cylinder are remarkably different. The velocity at the upper gap is higher than that at the lower side of the cylinder.

The contour plots in Fig. 2 show a high level of turbulence kinetic energy concentrated in the jet flow region, where the mean velocity is large. The maximum velocity of the flow in the jet region is almost four times greater than the free stream flow speed, and the jet flow region also exhibits the highest levels of velocity fluctuations. Detailed discussion of these flow phenomena and the gap ratio effect are given in Daichin and Lee (2001).

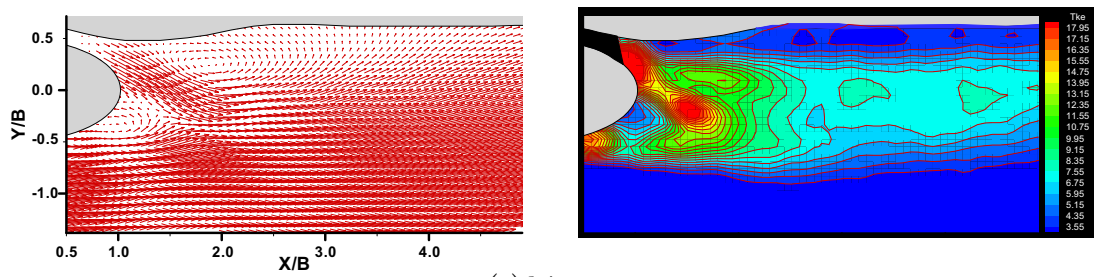

(a) h*=0.3

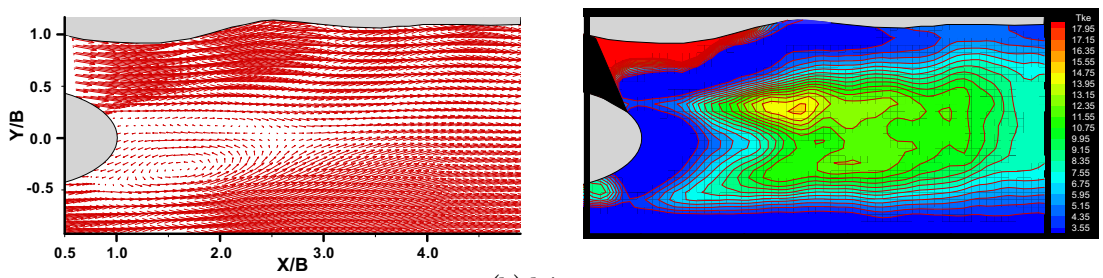

(b) h*=0.6

Fig. 2. Mean velocity fields and the turbulence kinetic energy.

4.1 Eigenvalues

The eigenvalues and eigenmodes were calculated for the flow fields at gap ratios of **h***=0.3 and 0.6; Fig.3 shows the convergence of the accumulated eigenvalues for each gap ratio. In this figure, k is the eigenmode, N is the total number of eigenmodes, and λ and λ_t are the accumulated eigenvalue and total eigenvalue respectively. The dominant POD modes, which represent the large-scale turbulent structure embedded in the flow field, are those with the highest kinetic energy.

The convergence of the POD eigenvalue is defined in terms of the ratio of the energy contained in the kth mode to the total energy in the flow field, i.e., the contribution of each mode to the total kinetic energy. As shown in Fig.3(a), the convergence curve calculated from N=400 instantaneous velocity fields increases rapidly at small values of k/N. This sharp increase indicates that the lower modes contain most of the kinetic energy. The magnitude of the first eigenvalue, λ_0, is almost the same at the two gap ratios; these data imply that, regardless of the depth of cylinder submergence, the first eigenvalue accounts for about 75% of the total kinetic energy of the flow. Thus, the first eigenmode acts as the carrier of the flow. The second mode contains about 7% of the total kinetic energy, and the third mode has only 1~2%. The higher eigenmodes have even smaller eigenvalues and contain less energy, indicating that they contain information on smaller-scale flow structures.

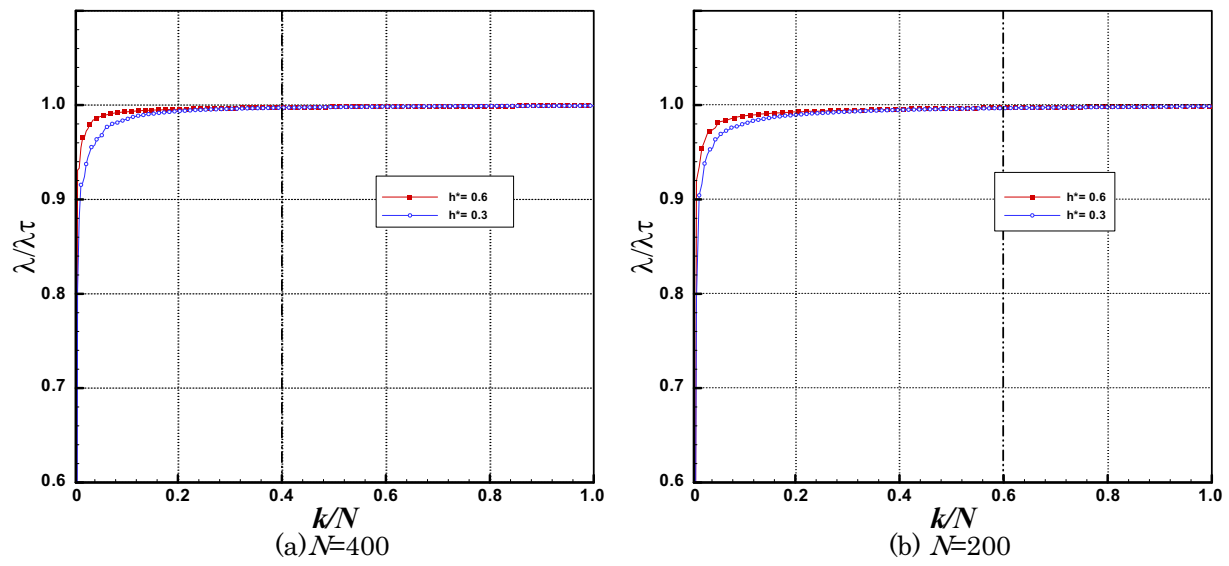

(a) N=400 (b) N=200

Fig. 3. The convergence of the normalized eigenvalue.

The ratio λ/λ_t for the larger gap ratio (h*=0.6) system increases rapidly at the initial, smaller eigenmodes and then quickly converges onto the curve for the small gap ratio (h*=0.3) system. This behavior implies that, for the larger gap ratio, most of the kinetic energy is contained in the lower eigenmodes. On the other hand, for the system with a smaller gap ratio, the large-scale flow structure spreads to higher eigenmodes, and small-scale fluctuations in the higher modes contribute to a greater extent to the global flow, compared with the h*=0.6 case.

To reduce the computation time, the *snapshot method* was employed in the present work instead of the *direct method*. However, even using the snapshot method, the POD analysis still required huge computation time to perform the matrix calculations for the large numbers of snapshots considered here. In practice, the choice of the number of the snapshots (instantaneous velocity fields) is very important because it is closely linked with the matrix size. The results of eigenvalues depend on the number of snapshots. If the accumulated eigenvalues obtained using a smaller number of snapshots begin to converge, then reliable POD results can be obtained with less computation time. For comparison with the data obtained using 400 snapshots (Fig.3(a)), the accumulated eigenvalues obtained from 200 snapshots were calculated (Fig.3(b)). The curves obtained from 200 snapshots converge slightly slower than those obtained from 400 snapshots; this tendency is particularly noticeable for the h*=0.6 system. Both curves obtained from 200 snapshots converge at about k/N=0.6, corresponding to mode 120, which is lower than the case of 400 snapshots, for which the two curves converge at about k/N=0.4, corresponding to mode 140. The results show

that, although the number of snapshots was halved, the eigenvalue convergence behavior was affected only slightly, and the fraction of the kinetic energy accounted for by the first several modes was similar. Thus, by reducing the number of snapshots, the eigenvalues start converging in a lower mode compared with calculations using a larger number of snapshots, and the overall computation time can be reduced.

4.2 Eigenmodes

The first four eigenmodes of the velocity field of the h*=0.3 system are shown in Fig.4. Each eigenmode represents a different flow structure embedded in the global flow field. As mentioned above, the first eigenmode (mode 0) represents the most energetic flow structure containing the greatest amount of kinetic energy. Therefore, the first eigenmode closely resembles the ensemble averaged velocity field shown in Fig. 2(a). For the h*=0.3 system, the stagnation point (marked by a square) is located at the lower side of the cylinder between the jet flow and the counter-clockwise vortex. In the second mode (mode 1), the counter-clockwise vortex under the jet flow has become diffuse, and another clockwise rotating vortex appears in the region where the stagnation point occurs in mode 0. Also in mode 1, the vortex between the jet and the free surface is stretched along the horizontal direction; this phenomenon seems to be the component of the flow pattern that is mainly responsible for the reverse flow motion near the free surface observed in the global flow field in Fig. 2(a). This reverse flow motion results from the fact that, in this mode, the vectors in the negative x direction near the free surface have much larger values than those in the mean velocity field. In the third mode (mode 2), two small-scale counter-rotating vortices are observed under the free surface, and the large-scale vortex under the down-washing jet flow, observed in the first and second modes, has nearly disappeared. In general, mode 3 displays a flow pattern similar to that of mode 2, but with the additional small-scale vortices under the free surface. The flow structures of modes 2 and 3 are quite different from the mean velocity field in the region between the free surface and the jet flow. The higher modes contain more detailed small-scale flow structure, in which the kinetic energy is relatively low.

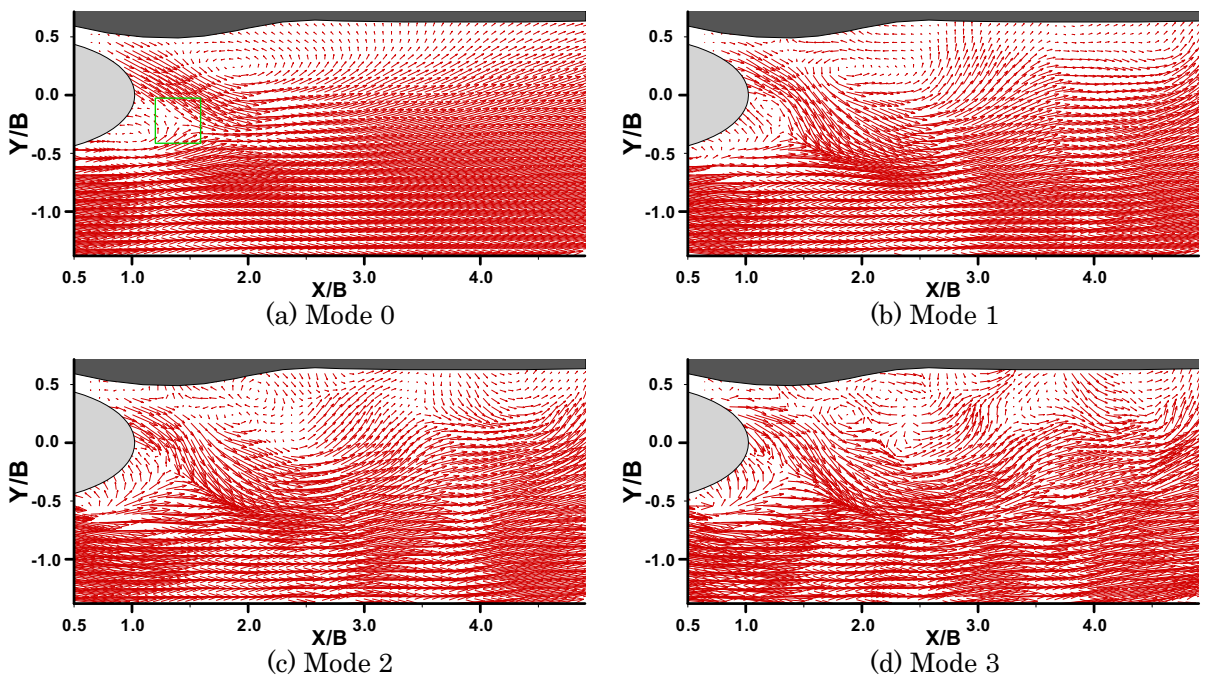

(a) Mode 0 (b) Mode 1

(c) Mode 2 (d) Mode 3

Fig. 4. The first four eigenmodes of POD analysis for gap ratio h*=0.3.

The higher eigenmodes extracted using the POD analysis provide the contributions of small-scale motions with active velocity fluctuations. For example, the jet flow for the first mode keeps concentration before merging into the free stream and the global flow field shows smooth variation. However, the higher modes show the spreading of the jet flow before it converges into the

free stream flow, with the degree of vertical motion diminishing as the velocity fluctuations increase. This is in good agreement with the mean turbulent kinetic energy distribution (Fig.2), in which the region of maximum kinetic energy coincides with the region where the jet flow merges with the free stream. The flow is highly turbulent, especially in the region near the free surface.

The large-scale flow structures of the first four eigenmodes are, in general, quite similar. This indicates that the high speed flow regions, such as in the jet flow and the free stream flow, contain the dominant flow phenomena with most of the kinetic energy. However, the structures of the low-velocity regions (on both sides of the jet flow) vary markedly from mode to mode, indicating that they are closely related with small-scale velocity fluctuations and the dynamics of the downstream flow field.

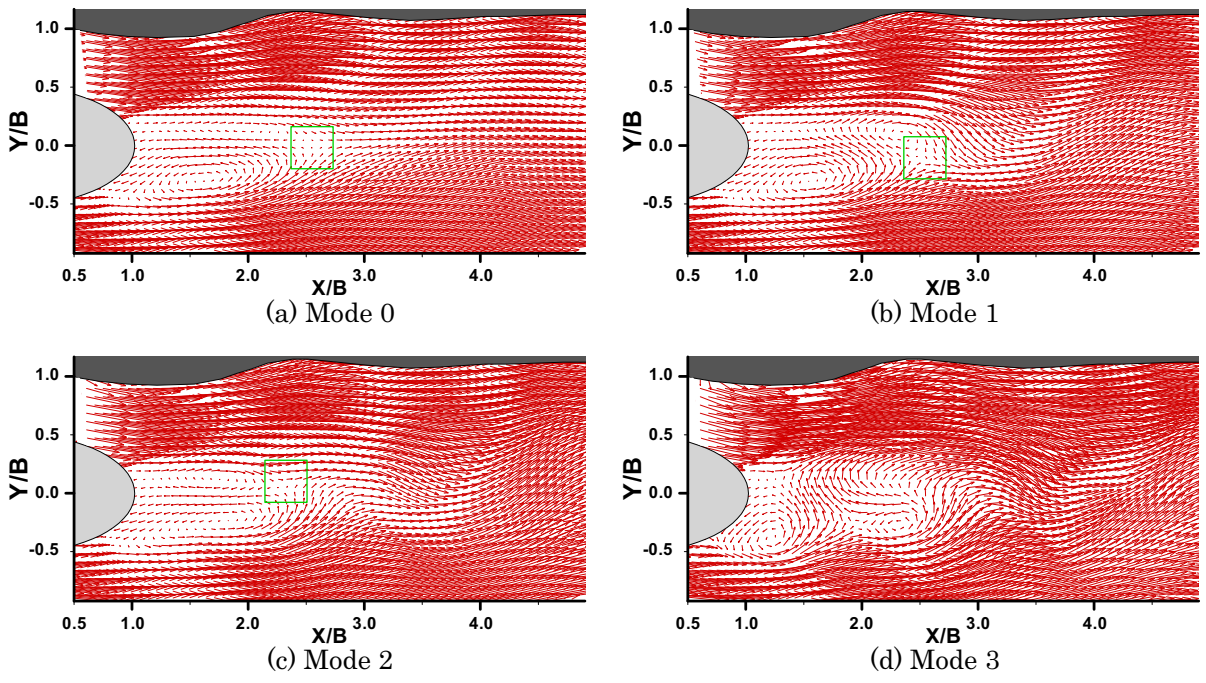

(a) Mode 0 (b) Mode 1

(c) Mode 2 (d) Mode 3

Fig. 5. First four eigenmodes for gap ratio h*=0.6.

For the h*=0.6 system, the high-speed gap flow above the cylinder suppresses the upper vortex and causes the flow velocity at the two sides of the cylinder to become asymmetric. For all eigenmodes (Fig. 5), the lower vortex dominates the wake region. For mode 0, the stagnation point (marked by a square box) is located on the cylinder major axis at X=1.5B. Mode 1 shows two counter-rotating vortices, situated asymmetrically in the near wake region. The presence of a small vortex at the right-upper side of the lower vortex causes the stagnation point to shift downward. Interestingly, although the stagnation point moves vertically, it barely shifts in the *x*-direction. Mode 2 shows an almost symmetric vortex structure in the near wake region. The size of the upper vortex is much larger than in mode 0. In addition, the lower vortex is spread along the *x*-direction, and the location of its core is further from the cylinder than in mode 0. In contrast to mode 1, the stagnation point in mode 2 is at almost the same vertical location as in mode 0, but it is displaced toward the cylinder along the *x*-direction. Therefore, modes 1 and 2 seem to be responsible for the vibration of the stagnation point in the *y*- and *x*-directions respectively. The combined effect of these two modes is to provoke fluctuations of the stagnation point in the flow. Mode 3 displays a more complicated flow structure; it contains two vortices in the lower wake region, and a series of vortices in the upper wake region that are indistinct due to vortex breakdown. For all eigenmodes, the contribution of the vortex structure in the lower wake region is stronger than that in the upper wake region due to the presence of the free surface and the strong gap flow above the cylinder. In addition, for each eigenmode, the kinetic energy contribution in the near-wake region changes substantially on increasing the gap ratio from h* = 0.3 to 0.6.

5. Conclusions

In the present study, POD analysis, an efficient tool for extracting the dominant coherent structures embedded in a flow field, was used to investigate the eigenvalues and eigenmodes of the near wake flow of an elliptic cylinder near a free surface. Comparison of the convergence of the accumulated eigenvalues calculated from 200 and 400 snapshots showed that, although the POD results depended somewhat on the snapshot number, the accumulated eigenvalues still converged using 200 snapshots, yielding valid results in much less computation time. The first four eigenmodes of the near wake behind the elliptic cylinder clearly showed the large-scale coherent structure at different energy levels. The majority of the kinetic energy was concentrated in the large-scale motions in the first and second eigenmodes. The higher eigenmodes provided more details on small-scale structures, most of which were located in the region of the mean velocity field exhibiting lower turbulence kinetic energy levels.

References

Choi J.H. and Lee S.J., Ground effect of flow around an elliptic cylinder in a turbulent boundary layer, J. of Fluids and Structures, 14(2000), 697-709.

Daichin and Lee S.J., Flow structure of the wake behind and elliptic cylinder close to a free surface, KSME Int. Journal, 15-12(2001), 1207-1216.

Craftieaux L., Michard M. and Grosjean N., Combining PIV, POD and vortex identification algorithms for the study of unsteady turbulent swirling flows, Meas. Sci. Technol., 12(2001), 1422-1429.

Lumley J.L., holmes P. and Berkooz G., The proper orthogonal decomposition in the analysis of turbulent flows, Ann. Rev. Fluid Mech., 25(1993), 539-575.

Lumley J.L., holmes P. and Berkooz G., Turbulence, coherent structures, dynamical systems and symmetry, (1996), Cambridge University Press.

Modi, V. J. and Wiland, E., Unsteady aerodynamics of stationary elliptic cylinders in subcritical flow, AIAA J., 8(1970), 1814-1821.

Patte-rouland B., Lalizel G., Moreau J. and Rouland E., Flow analysis of an annular jet by particle image velocimetry and proper orthogonal decomposition, Meas. Sci. Technol., 12(2001), 1404-1412.

Pedersen J.M., and Meyer K.E., POD analysis of flow structures in a scale model of a ventilated room, Exp. in Fluids, 33(2002), 940-949.

Shin, D.S. and Lee, S.J., Velocity field measurements of flow inside Snout of continuous hot-dip galvanizing process using a single-frame PIV technique, ISIJ Int., 40(2000), 484-490.

Sirovich L., Turbulence and the dynamics of coherent structures. Par 1: coherent structures, Q Appl. Math., 45(1987), 561-571.

Author Profile

Daichin (Dai Qin): He received his MSc from Inner Mongolia University (China) and his Ph.D. in Offshore Engineering from Dalian University of Technology, China in 1998. He worked as a post-doctoral researcher at the Institute of Fluid Mechanics, BUAA (Beijing University of Aeronautics and Astronautics) from 1998 to 2000. Since then he has worked as a post-doctoral researcher at the Department of Mechanical Engineering, Pohang University of Science and Technology (POSTECH). His research interests include flow visualization, the PIV technique, and bluff-body hydro/aero dynamics.

Sang Joon Lee: He received his MSc and Ph.D. in Mechanical Engineering from KAIST (Korea Advanced Institute of Science and Tech.) in 1982 and 1986, respectively. In 1986 he worked as a senior researcher at KIMM. He joined the Department of Mechanical Engineering at POSTECH as an Assistant Professor in 1987, and in 1999 he became a full professor. His research interests include quantitative flow visualization (PIV, PTV, LIF, and Holography), experimental fluid mechanics, bluff body aerodynamics, microfluidics and flow control.